Interpreting TMEM67 missense variants of uncertain significance (VUS) in an animal model

Karen I. Lange[1*], Sunayna Best[2], Sofia Tsiropoulou[1], Ian Berry[3], Colin A. Johnson[2], Oliver E. Blacque[1*]

1. School of Biomolecular and Biomedical Science, Conway Institute, University College Dublin, Ireland.
2. Division of Molecular Medicine, Leeds Institute of Medical Research, University of Leeds, Leeds, West Yorkshire, UK.
3. Bristol Genetics Laboratory, Pathology Sciences, Southmead Hospital, Bristol, BS10 5NB, UK.

* Correspondence to karen.lange@ucd.ie, oliver.blacque@ucd.ie

Keywords: *C. elegans,* CRISPR, *TMEM67, mks-3*, Meckelin, disease modelling, VUS interpretation, ciliopathy, Meckel Syndrome, Joubert Syndrome, COACH.

ABSTRACT

Purpose:A molecular genetic diagnosis is essential for accurate counselling and management of patients with ciliopathies. Uncharacterized missense alleles are often classified as variants of uncertain significance (VUS) and are not clinically useful. In this study, we explore the use of a tractable animal model (*C. elegans*) for *in vivo* interpretation of missense VUS alleles of *TMEM67*, a gene frequently mutated as a cause of ciliopathies.

Methods: CRISPR/Cas9 gene editing was used to generate homozygous worm strains carrying *TMEM67* patient variants. Quantitative phenotypic assays (dye filling, roaming, chemotaxis) assessed cilia structure and function. Results were validated by genetic complementation assays in a human *TMEM67* knock-out hTERT-RPE1 cell line.

Results: Quantitative assays in *C. elegans* distinguished between known benign (Asp359Glu, Thr360Ala) and pathogenic (Glu361Ter, Gln376Pro) variants. Analysis of seven missense VUS alleles predicted two benign (Cys173Arg, Thr176Ile) and four pathogenic variants (Cys170Tyr, His782Arg, Gly786Glu, His790Arg). Results from one VUS (Gly979Arg) were inconclusive in worms, but additional *in vitro* validation suggested it was likely benign.

Conclusion: Efficient genome editing and quantitative functional assays in *C. elegans* make it a tractable *in vivo* animal model that allows stratification and rapid, cost-effective interpretation of ciliopathy-associated missense VUS alleles.

INTRODUCTION

Whole exome and genome sequencing has revolutionised our ability to identify the genetic causes of disease, interrogate disease mechanisms and pinpoint gene targets for therapy. A molecular genetic diagnosis for inherited disorders informs patient care, facilitates accurate genetic counselling and cascade family testing, and qualifies individuals for gene-specific clinical trials[1,2] thereby underpinning personalized medicine approaches to individual clinical management. However, the abundance of genomic sequencing data has led to a major bottleneck in the interpretation of identified variants as either pathogenic or benign. Missense mutations, where a single codon is altered to encode a different amino acid, are the most numerous class of protein-altering mutations[3]. However, only a subset of missense variations are associated with disease[4]. For most rare missense variants, the only lines of available evidence are that the variant is absent from population controls and/or *in silico* tools support a deleterious effect, which together are not enough to meet the threshold for a 'likely pathogenic' classification. These are classified as variants of uncertain significance (VUS)[5,6]; most variants across all disease genes are currently classified as VUS[7]. In general, VUS are not clinically actionable. Clearly, better tools are required to allow more definitive interpretation of genetic variants. Given the wealth of genomic data now available, there is a pressing clinical need to provide systematic functional interpretation of VUS since this is essential for accurate molecular genetic diagnosis. For functional testing to be incorporated into standard variant interpretation and to be deliverable in the mainstream clinical setting, it needs to be accurate, quick, affordable, and easily interpretable. Achieving this is a priority in this genomics era to gain maximum benefit from available data.

Whilst many *in silico* prediction algorithms have been developed, their accuracy for interpreting the pathogenicity of missense variants is inconsistent[8–10]. This has led to the urgent need to develop effective new strategies for the functional interpretation of missense variants[11]. To this end, non-rodent model organisms such as zebrafish, *Drosophila* and *C. elegans* are emerging as robust *in vivo* experimental platforms for determining the pathogenicity of variant mutations[12,13]. This is because gene manipulation and complementation-based technologies have advanced rapidly and many human disease genes are highly conserved orthologues in these organisms, functioning within conserved pathways.

Furthermore, the orthologous proteins frequently display high amino acid sequence identity to the human orthologue, thereby allowing specific variation such as missense mutations to be modelled.

Ciliopathies are a heterogenous group of at least 25 inherited disorders with clinically overlapping phenotypes, caused by mutations in more than 190 causative genes[14]. These diseases affect many organ systems, causing a broad range of clinical phenotypes of varied severity and penetrance that include cystic kidneys, retinal dystrophy, bone abnormalities, organ laterality defects, respiratory tract defects, infertility, obesity, neurodevelopmental defects and cognitive impairment[15]. Ciliopathies are caused by defects in motile or non-motile (primary) cilia, which are microtubule-based organelles, typically 2-20 microns long, that extend from the surfaces of most cell types. Whilst motile cilia propel cells through a fluid or push fluid across a tissue surface, primary cilia act as cellular "antennae"[16], transducing a wide variety of extrinsic chemical and physical (eg. light, odorants) signals into the cell[17]. Primary cilia are especially important for coordinating several cell-cell communication signaling pathways (eg. Shh, Wnt, PDGF-a) essential for tissue development and homeostasis[18].

In this study, we examine the use of the nematode *Caenorhabditis elegans (C. elegans)* to interpret VUS mutations associated with ciliopathies. *C. elegans* is a leading model for investigating cilia biology and ciliopathy pathomechanisms, with many ciliopathy genes and associated pathways conserved in worms[19]. Advances in genome editing in *C. elegans* provide an excellent opportunity to model ciliopathy variation. Indeed, we recently showed that we can model known pathogenic missense ciliopathy mutations in *C. elegans*, and accurately assess their effects on underlying gene function using quantitative assays of cilium structure and cilia-dependent sensory behaviours[20].

TMEM67 is a transmembrane protein that localizes very specifically to the most proximal 0.2-1.0 μm region of the ciliary axoneme called the transition zone (TZ)[21,22]. Mutations in *TMEM67* cause several autosomal recessive ciliopathies[23] with overlapping phenotypes that include Joubert syndrome (OMIM#610688), Meckel syndrome (OMIM#607361), nephronophthisis (OMIM#613550), COACH syndrome (OMIM#216360), and RHYNS

syndrome (OMIM#602152). Variants in *TMEM67* have also been identified in patients with non-syndromic conditions including cystic kidney disease[24] and congenital liver fibrosis[25]. More than 60% of reported missense variants in *TMEM67* have uncertain or conflicting interpretations of their clinical significance (84/137=61.3%, accessed from ClinVar[26] on April 17, 2021). The abundance of human VUS alleles makes *TMEM67* an excellent candidate to explore if modelling VUS in *C. elegans* can generate evidence about their pathogenicity.

Here, we used CRISPR-Cas9 knock-in technology to model seven TMEM67 VUS missense mutations at the orthologous residue in the *C. elegans* orthologue (MKS-3). Using quantifiable assays of cilium/TZ structure and function, we determined whether the variants are damaging or benign with respect to both *mks-3* gene function and to the TZ localisation of the MKS-3 protein. We then validated the nematode findings using a genetic complementation-based approach in *TMEM67*-disrupted human cells. In summary, our study indicates that *C. elegans* is a tractable model system that can rapidly provide evidence for the interpretation of ciliopathy VUS.

METHODS

C. elegans maintenance

All *C. elegans* strains in this study were maintained at 20ºC or 15ºC on nematode growth medium seeded with OP50 *E. coli* using standard techniques[27]. All worm strains generated or used in this study are listed in Table S2.

CRISPR/Cas9 to engineer *mks-3* mutants in *C. elegans*

All CRISPR protocols were performed as previously described[20] in *nphp-4(tm925)*. The only deviation was that up to three repair templates were added to a single Cas9 injection mix if multiple variants could be targeted by one crRNA (Table S3). The CRISPR efficiency varied from 2-60% with an average 20%. Accuracy of the mutations was confirmed with Sanger sequencing. PCR primers used to detect, sequence, and genotype the *mks-3* variants are listed in Table S4.

132 ***C. elegans* quantitative phenotyping assays**

133 Dye filling, roaming, chemotaxis, and osmotic avoidance assays were performed as
134 previously described[28]. All of these assays were performed blinded to genotype for at least
135 three independent biological replicates.

136

137 **Generating transgenic animals expressing MKS-3::GFP**

138 A PCR-based GFP fusion technique was used to generate the *mks-3::gfp* constructs[29]. gDNA
139 isolated from each of the mutant strains (including 485 bp upstream from the start codon) was
140 fused to GFP amplified from pPD95_77 (Addgene plasmid # 1495). All primers used in the
141 fusion PCRs are listed in Table S4. *mks-3(tm2547)* hermaphrodites were injected with
142 0.25ng/µl *mks-3::gfp* and 100ng/µl coel::dsRed (Addgene plasmid # 8938) to generate
143 extrachromosomal arrays (2-7 independent lines each). PCR was performed to confirm
144 *mks-3::gfp* was present.

145

146 ***C. elegans* wide-field imaging and quantification of fluorescence**

147 Young adult hermaphrodites were immobilised on 4% agarose pads in 40 mM tetramisole
148 (Sigma). Images were acquired with a 100x (1.40 NA) oil objective on an upright Leica
149 DM5000B epifluorescence microscope and captured with an Andor iXon+ camera run by
150 Andor software. Image analysis was performed with FIJI/ImageJ (NIH). MKS-3::GFP
151 fluorescence at the TZ was quantified as previously described[20].

152

153 **Transmission Electron Microscopy**

154 Young adult hermaphrodite worms were processed as previously described[28]. Briefly, worms
155 were fixed in 2.5% glutaraldehyde (Merck) in Sørensen's phosphate buffer (0.1 M, pH 7.4)
156 for 48 h at 4°C, post-fixed in 1% osmium tetroxide (EMS) for 1 h and dehydrated through an
157 increasing ethanol gradient. Samples were subsequently treated with propylene oxide (Sigma)
158 and embedded in EPON resin (Agar Scientific) for 24 h at 60°C. Serial, ultra-thin (90 nm)
159 sections of the worm nose tissue were cut using a Leica EM UC6 Ultramicrotome, collected
160 on copper grids (EMS), stained with 2% uranyl acetate (Agar Scientific) for 20 min followed
161 by 3% lead citrate (LabTech) for 5 min and imaged on a Tecnai 12 (FEI software) with an
162 acceleration voltage of 120 kV.

163

164 **Cell Culture**

165 Human hTERT-immortalized retinal pigmentary epithelial (hTERT-RPE1, American Type
166 Culture Collection; ATCC) wild-type and crispant cell-lines were grown in Dulbecco's
167 minimum essential medium (DMEM)/Ham's F12 medium supplemented with GlutaMAX
168 (Gibco #10565018) and 10% fetal bovine serum (FBS). For selected experiments involving
169 cilia, cells following passage were serum-starved in DMEM/F-12 media containing 0.2%
170 FBS. Cells were cultured in an incubator at 37˚C with 5% CO2.

171

172 **TMEM67 cloning, plasmid constructs and transfections**

173 The full-length ORF for *H. sapiens* TMEM67 isoform 1 (RefSeq JF432845, plasmid ID
174 HsCD00505975) was obtained from the DNASU Plasmid Repository cloned into the
175 pENTR223 Gateway donor/master vector. The ORF was Gateway cloned into a C-terminal
176 GFP-tagged Gateway pcDNA-DEST47 vector (ThermoFisher Scientific), sequence verified,
177 and then sub-cloned into the pcDNA3.1 myc/HisA vector by using HiFi cloning (New
178 England Biolabs Inc.) We also introduced an endogenous Kozak sequence prior to the start
179 site, the first 30 nucleotides of the main transcript that were missing from the DNASU
180 sequence, and a GS linker sequence between the end of the ORF and the myc tag. To
181 generate variants of interest within the TMEM67 insert, we used the QuikChange II XL
182 Site-Directed Mutagenesis Kit (Agilent) according to the manufacturer's protocol. Primers
183 were designed using the web-based QuikChange Primer Design Program
184 (https://www.agilent.com/store/
185 primerDesignProgram.jsp). Primer sequences are listed in Table S5. The final constructs were
186 verified by bidirectional DNA sequencing. For transfection with plasmids, cells at 80%
187 confluency were transfected using Lipofectamine 2000 (Life Technologies Ltd.) according to
188 the manufacturer's instructions and as described previously (Abdelhamed et al., 2015).

189

190 **CRISPR/Cas9 genome editing in cell culture**

191 GFP-expressing pSpCas9(BB)-2A-GFP (PX458) vector was the kind gift of Feng Zhang
192 (Addgene plasmid #48138). Three crRNAs targeting human TMEM67 (RefSeq
193 NM_153704.5) were designed using the online tool Benchling (see https://benchling.com),
194 selected for the highest ranking on- and off-target effects. crRNAs were ordered as high
195 performance liquid chromatography (HPLC)-purified oligos from Integrated DNA

196 Technologies (IDT) in addition to Alt-R CRISPR-Cas9 tracrRNA-ATTO550 conjugates.
197 crRNA sequences are listed in Table S6. Lyophilised pellets were resuspended in Tris-EDTA
198 (TE) buffer (Qiagen) to give 100mM stocks. crRNA and tracrRNA were mixed in a 1:1 ratio,
199 then incubated in nuclease-free duplex buffer (30 mM HEPES, pH 7.5, 100 mM potassium
200 acetate) to make 300nM guide RNA master mixes. Before transfecting into cells the
201 crRNA:tracrRNA duplexes were incubated with Lipofectamine 2000 at an
202 RNA:Lipofetamine ratio of 2:1 in 200µl/well Opti-MEM for 20 minutes. 1ml of media from
203 6-well plate wells was removed, the transfection reagents applied, and the cells were then
204 incubated overnight. Media was changed on the cells to fresh DMEM/F-12 with 10% FCS
205 after 16 hours, and the cells incubated for a total of 48 hours.
206
207 **Fluorescence-activated cell sorting (FACS)**
208 Following transfection, FACS was performed to enrich cells expressing GFP and to produce
209 clonal populations. 96 well plates (Corning) were treated with 200µl of 4% bovine serum
210 albumin (BSA) per well for one hour. Wells were then filled with 100µl of collection buffer
211 (20% FCS, 1% penicillin-streptomycin, 50% conditioned media, 29% fresh DMEM/F-12
212 media) that had been filter-sterilised. Transfected cells were prepared for FACS by removing
213 media, washing in PBS then treating with trypsin for 5 min before resuspending in
214 filter-sterilised sorting buffer (1x Ca^{2+}/Mg^{2+}-free PBS, 5mM EDTA, 25mM HEPES pH 7.0).
215 A 70µm filter was used to disperse cells into 4% BSA-treated polystyrene FACS tubes. A BD
216 Influx 6-way cell sorter (BD Biosciences) was used to index sort GFP-positive cells,
217 calibrated against un-transfected control cells. When an abundance of GFP positive cells
218 were present, the top 5% were targeted for index sorting. After sorting, cells were incubated
219 for 3 weeks at 37°C with 5% CO2, with weekly checks for growing colonies.
220
221 **PCR and sequence validation of mutations in crispant cell-lines**
222 To extract DNA from colonies within the 96-well plates, cells were washed with 1x
223 Ca^{2+}/Mg^{2+}-free PBS then resuspended in 50µl of DirectPCR Lysis Reagent (Viagen Biotech)
224 containing 0.4 mg/ml Proteinase K (Sigma, # P4850). Suspensions were incubated at 55°C
225 for 5 hours, followed by 85°C for 45 minutes. 1µl of DNA extracts were used in PCR
226 reactions that amplified sequences flanking the predicted edit sites in *TMEM67* exons 2, 3 or
227 5. Primers are listed in Table S7. Mutations were identified by Sanger sequencing (GeneWiz

228 Inc.) followed by analysis using the ICE v2 CRISPR Analysis Tool (see
229 https://www.synthego.com/products/bioinformatics/crispr-analysis). The following clones
230 were chosen for further study: clone 40, heterozygous for c.369delC (p.Glu124Lysfs*12); and
231 clone 16 carrying biallelic mutations [c.519delT]+[c.519dupT] ([p.Cys173Trpfs*20]+[
232 p.Glu174*]). All mutations were predicted to result in nonsense mediated decay by the
233 Ensembl Variant Effect Predictor program (VEP)
234 (https://www.ensembl.org/Homo_sapiens/Tools/VEP). Clone 21 was a negative control
235 cell-line that was mock-transfected, underwent FACS and index-sorting, but was verified to
236 carry normal wild-type *TMEM67* sequence.
237
238 **Antibodies**
239 The following primary antibodies were used: mouse anti-β actin (1:10000, clone AC-15,
240 Abcam Ltd., Cambridge, UK); rabbit polyclonal anti- MKS3/TMEM67 (1:500, 13975-1-AP;
241 ProteinTech Inc., Rosemont, IL, USA); goat anti-ROR2 (1:1000, AF2064; R&D Systems
242 Inc., Minneapolis, MN, USA).
243
244 **Whole cell extract preparation and western immunoblotting**
245 Whole cell extracts (WCE) containing total soluble proteins were prepared from
246 hTERT-RPE1 cells that had been transiently transfected with 1.0 µg plasmid constructs in
247 90mm tissue culture dishes, or scaled down as appropriate. Ten µg WCE total soluble protein
248 was analysed by SDS-PAGE (using 4-12% polyacrylamide gradient gels) and western
249 blotting according to standard protocols using either rabbit polyclonal antisera (final dilutions
250 of 1:200-1000) or mAbs (1:1000-5000). Appropriate HRP-conjugated secondary antibodies
251 (Dako UK Ltd.) were used (final dilutions of 1:10000-25000) for detection by the enhanced
252 chemiluminescence "Femto West" western blotting detection system (Thermo Fisher
253 Scientific Inc., Rockford, IL, USA) and visualized using a ChemiDoc MP imaging system
254 (BioRad Inc., Hercules, CA, USA). Ratios of active phosphorylated ROR2 :
255 unphosphorylated ROR2 isoforms were calculated by quantitating band intensity using
256 ImageLab 5.2.1 software (BioRad Inc.) for three independent biological replicate
257 experiments, as described previously[30].
258
259 **Modelling of protein secondary structure**

Full-length human TMEM67 isoform 1 protein sequence (NP_714915.3) and *C. elegans* MKS-3 (NP_495591.2) were analysed by the RaptorX protein structure prediction server (http://raptorx.uchicago.edu/), using default settings for the deep dilated convolutional residual neural networks method[31]. Absolute model quality was assessed by ranking GDT (Global Distance Test) scores defined as 1*N(1)+0.75*N(2)+0.5*N(4)+0.25*N(8), where N(x) is the number of residues with estimated modelling error (in Å) smaller than x, divided by protein length and multiplied by 100. The highest ranking model for human TMEM67 had overall GDT = 28.968 (with values >50 an indicator of good model quality), indicating that portions of the model are lower quality. The best model for worm MKS-3 had GDT = 19.269. Predicted models in the .pdb format were visualized and annotated in EzMol (http://www.sbg.bio.ic.ac.uk/ezmol/).

Statistical analyses

Results reported are from at least three independent biological replicates. All graphs and statistical analyses of *C. elegans* data sets were performed in Microsoft Excel with the Real Statistics Resource Pack Version 7.2 (www.real-statistics.com). A Shapiro-Wilk test was used to calculate if the data were normally distributed. Statistical significance was determined with an ANOVA followed by Tukey's *post hoc* (chemotaxis and GFP quantification) or Kruskal-Wallis followed by Dunn's (roaming) or Schaich-Hammerle (dye filling) *post hoc* tests. For all phenotypic assays statistical significance of the variants was determined relative to the *nphp-4* single mutants. For cell culture results, a normal distribution of data was confirmed using the Kolmogorov-Smirnov test (GraphPad Prism, GraphPad Software Inc., La Jolla, CA, USA). Pairwise comparisons were analysed with Student's two-tailed t-test using InStat (GraphPad Software Inc.). *, **, and *** refer to p-values of <0.05, <0.01, and <0.001, respectively.

RESULTS

Selection of TMEM67 variants for analysis

In this study we aimed to model ciliopathy-associated variants of uncertain significance (VUS) in *C. elegans* to generate *in vivo* evidence about the pathogenicity of the alleles. Specifically, we focussed on seven missense VUS alleles of *TMEM67* (**Figure 1A, Table S1**).

A

	MKS-3	TMEM67
Benign1	D265E	D359E
Benign2	S266A	T360A
Pathogenic1	L267*	E361*
Pathogenic2	K281P	Q376P
VUS1	C115Y	C170Y
VUS2	C118R	C173R
VUS3	S121I	T176I
VUS4	H683R	H782R
VUS5	G687E	G786E
VUS6	H691R	H790R
VUS7	S882R	G979R

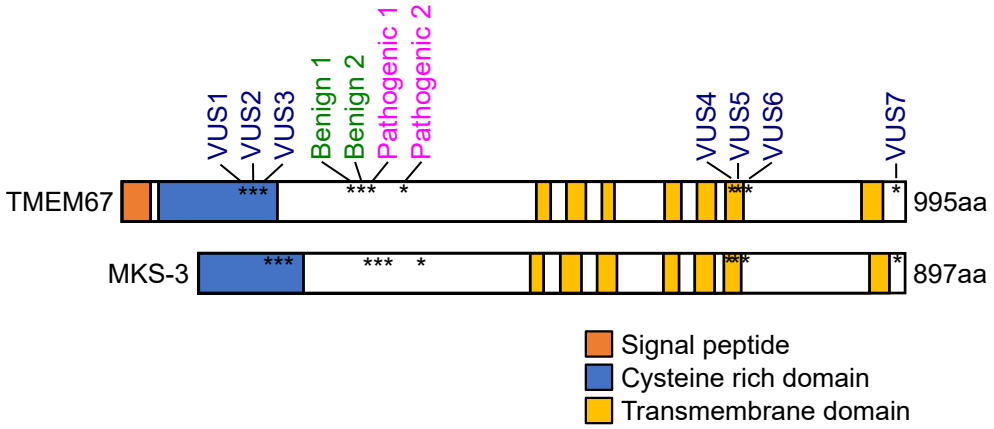

B

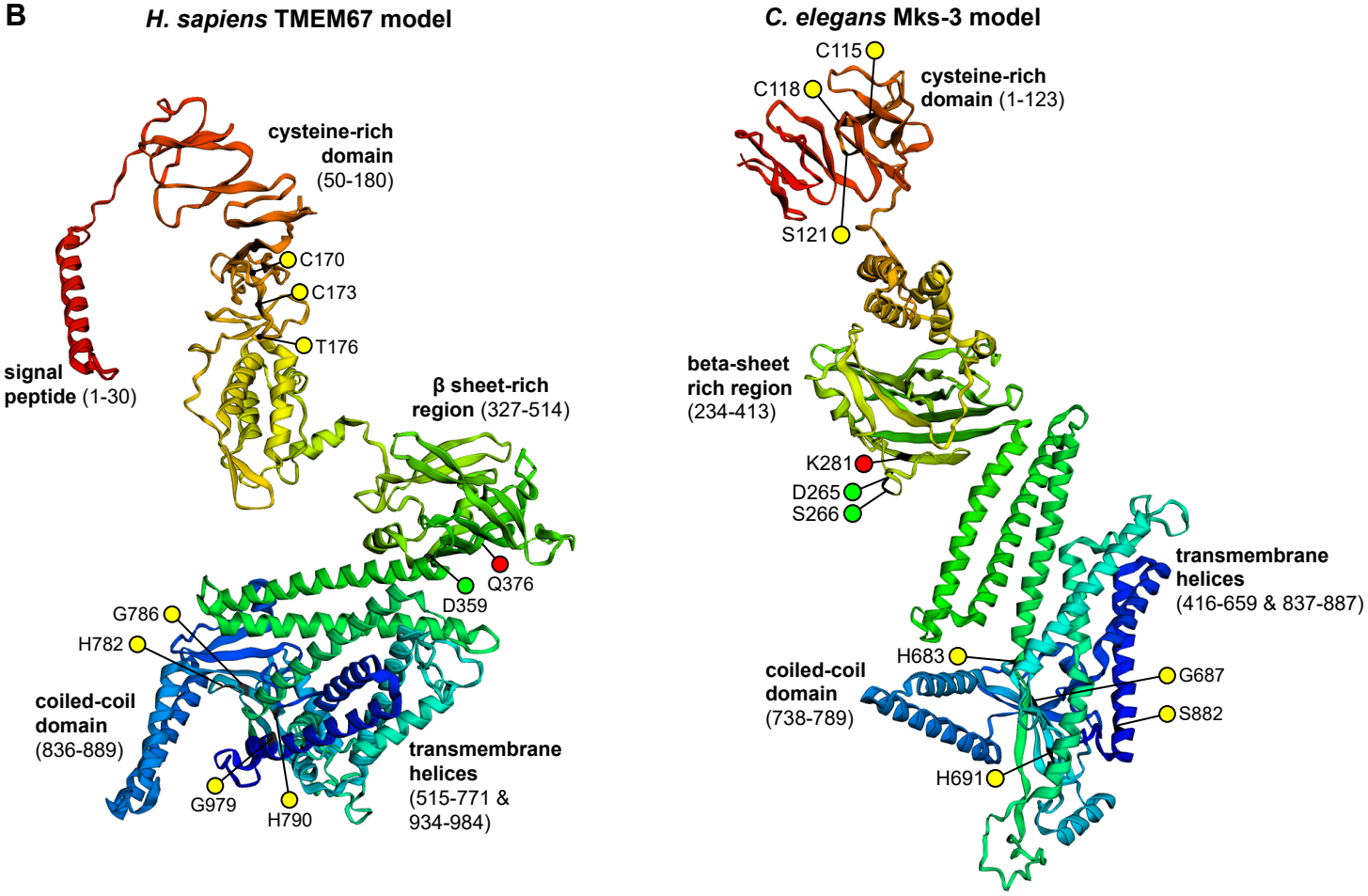

Figure 1. *TMEM67* variants analyzed in this study

A) Eleven variants in *TMEM67/mks-3* were generated by CRISPR-Cas9 gene editing and characterized in C. elegans. The schematic shows the relative positions of the variants along the length of the proteins. The domains are conserved between humans and worms, but the worm protein lacks the N-terminal signal peptide.

B) RaptorX protein structure and domain organization predictions for the full-length TMEM67 and MKS-3 proteins. RaptorX is a deep learning algorithm that predicts secondary and tertiary structures of proteins without close homologues or known structures in the protein data bank. Ribbon diagrams of proteins are rainbow-coloured (red at N-terminus to dark blue at C-terminus) with variants indicated (red, known pathogenic; yellow, VUS; green, known benign) within the predicted protein domains. Note that transmembrane helices 1-5 (green to cyan) are followed by a single coiled-coil domain (light blue) and then two C-terminal transmembrane helices 6-7 (dark blue).

292 Variants were selected using two criteria: (i) conservation, or near conservation (closely
293 related residue), of the mutated amino acid in the *C. elegans* orthologue, within a conserved
294 domain/region of the protein (**Figure S1**), and (ii) the requirement of an adjacent Cas9 PAM
295 site in the *C. elegans* genome. MKS-3, the *C. elegans* ortholog of TMEM67, has 45.5%
296 amino acid similarity (**Figure S1**). VUS1(C170Y), VUS3(T176I), VUS6(H790R), and
297 VUS7(G979R) were identified from clinical exome sequencing of Meckel syndrome
298 foetuses. VUS2(C173R), VUS4(H782R) and VUS5(G786E) were selected from publicly
299 available databases. We also included two known benign and two pathogenic variants as
300 controls. Benign1(D359E) was identified on the Ensembl variation database[32].
301 Benign2(T360A), Pathogenic1(E361*), and Pathogenic2(Q376P) on ClinVar[26]. For clarity,
302 we refer to the variants in this manuscript using a simplified notation (e.g. Benign1,
303 Pathogenic1, VUS1). A *de novo* protein structure prediction program, Raptor X, revealed that
304 the human and worm TMEM67 proteins had remarkable similarities in their overall predicted
305 domain organization and secondary structure. The targeted pathogenic, benign and VUS
306 residues were present in comparable regions of secondary structure (**Figure 1B**), with
307 residues associated with known benign variants in exposed loops of the proteins whereas
308 known pathogenic missense mutations were buried in β-sheets (**Figure S2**).
309

310 **Quantitative phenotypic analysis of *mks-3* VUS alleles in *C. elegans***

311 We employed a CRISPR/Cas9 genome editing methodology[20] to engineer homozygous
312 worms with mutations in *mks-3* that correspond to the *TMEM67* variants (**Figure 1**). Since
313 *mks-3* functions redundantly with NPHP module genes (*nphp-1/4*) to regulate ciliary/TZ
314 structure and function, we generated the *mks-3* variants in an *nphp-4(Δ)* mutant background
315 to facilitate quantitative phenotypic analysis[22]. To determine the precise effect of the knock-in
316 mutations on underlying *mks-3* gene function, we employed well-established, robust and
317 highly quantitative assays of ciliary/TZ structure and function. Double mutant
318 *mks-3(variant)*; *nphp-4(Δ)* phenotypes were compared to *mks-3(+); nphp-4(Δ)* (positive
319 control) and *mks-3(Δ)*; *nphp-4(Δ)* (negative control; deletion allele in *mks-3*)[22]. We expected
320 that pathogenic alleles would be phenotypically similar to the reference *mks-3(Δ)* allele.
321

322 The dye filling assay indirectly assesses the structural integrity of cilia. When worms are
323 placed in a DiI or DiO solution, the fluorescent dye incorporates into the membranes of 16

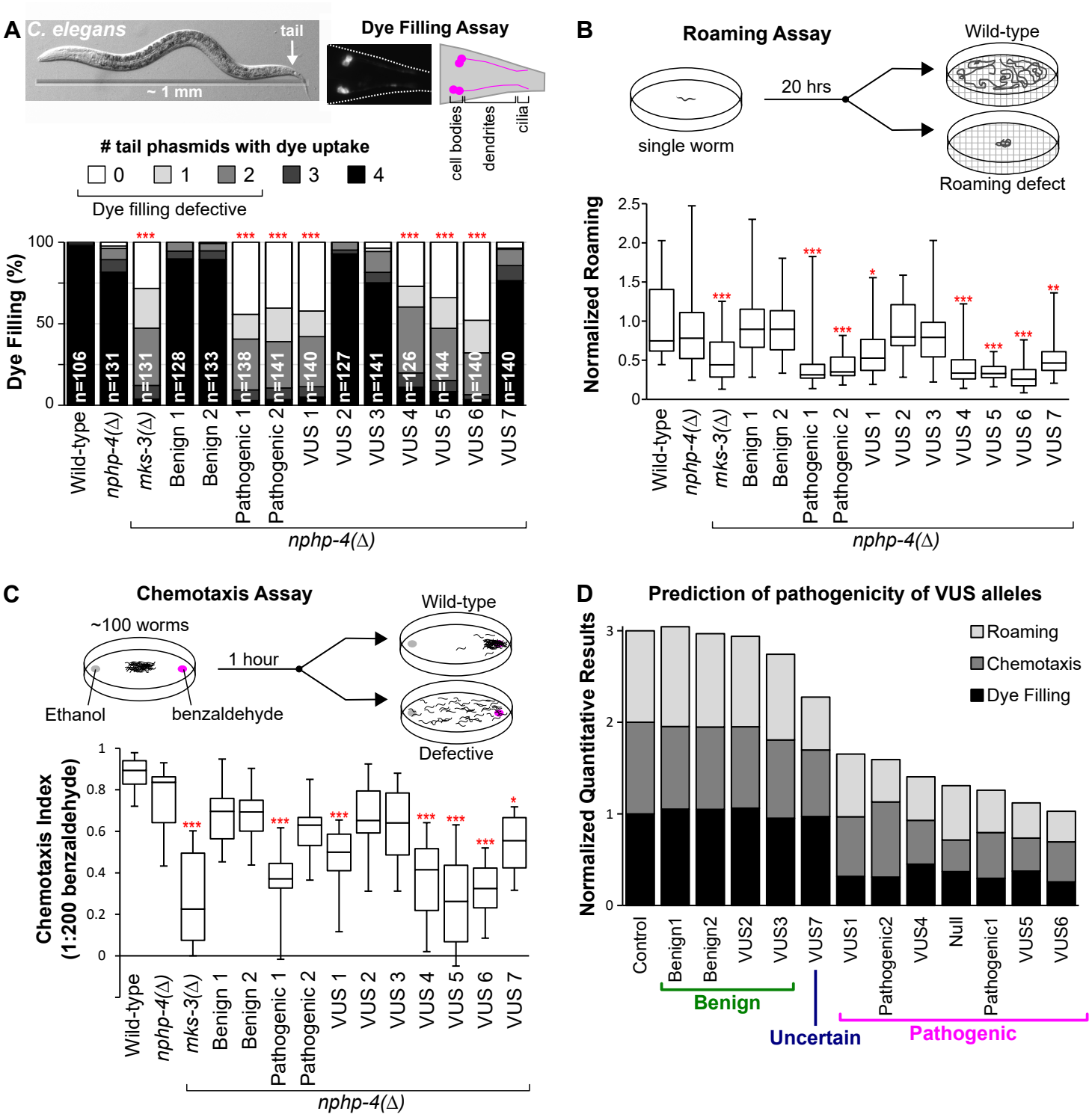

Figure 2. Quantitative phenotyping of cilia-dependent phenotypes in *C. elegans*

A) Lipophilic dye filling assay of the four phasmid (tail) neurons. The number of cell bodies which uptake dye was counted (values range from 0-4). The bar graph indicates the proportion of the population that were dye filling defective (≤ 2 phasmid cell bodies with dye uptake). n>100 worms for each genotype. Statistical significance according to Kruskal-Wallis followed by Schaich-Hammerle *post hoc* test.

B) Assessment of worm roaming behaviour normalised to wild-type. A single young adult hermaphrodite was placed on a food rich plate for 20 hours and the roaming activity was quantified. n=30 worms for each genotype. Statistical significance according to Kruskal-Wallis followed by Dunn's *post hoc* test.

C) Quantification of worm chemotaxis towards benzaldehyde after 60 minutes. Assay is performed on a population of 50-200 worms. n=16-25 trials for each genotype. Statistical significance according to ANOVA followed by Tukey's *post hoc* test. Box plots indicate the maximum and minimum values (bars), median, lower quartile, and upper quartile.

D) Integration of the phenotypic results from the three quantitative assays into one value. Averages from each assay were normalized to the nphp-4 control and summed. Values were ranked from highest (benign) to lowest (pathogenic).

environmentally-exposed amphid (head) and phasmid (tail) sensory cilia before rapidly diffusing to the entire neuronal plasma membrane[28,33]. Neuronal dye filling defects strongly correlate with abnormalities in cilium structure[34]. Here, we assessed DiI/DiO staining in the four ciliated phasmid sensory neurons in the tail. Wild type and *mks-3(+)*; *nphp-4(Δ)* positive controls display robust dye filling, whereas *mks-3(Δ); nphp-4(Δ)* negative controls are dye filling defective (**Figure 2A**). Like the positive controls, the Benign1 and Benign2-containing strains show robust dye uptake whilst those with Pathogenic1 and Pathogenic2 are defective (**Figure 2A**). Four of the VUS alleles cause a severe dye filling defect (VUS1/4/5/6), whereas three (VUS2/3/7) do not (**Figure 2A**). We further investigated the dye filling of the latter three putative benign alleles using a genetic complementation test with the *mks-3(Δ)* allele. Wild-type, Benign1, VUS2, VUS3, and VUS7 all complement the *mks-3(Δ)*-associated dye filling phenotype, whilst Pathogenic2 does not (**Figure S3**). This confirms that VUS2, VUS3, and VUS7 are phenotypically benign with regards to dye filling.

C. elegans foraging behaviour in a food rich environment is dependent on various sensory cilia[33]. In this assay a single young adult worm is placed on a lawn of bacteria for 20 hours and the extent of its roaming across the plate is determined by their visible tracks (**Figure 2B**). *mks-3(+); nphp-4(Δ)* worms show a slight decrease in roaming compared to wild-type worms, whereas *mks-3(Δ)*; *nphp-4(Δ)* worms exhibit a roaming defect (**Figure 2B**). As expected, Benign1 and Benign2-containing strains are roaming normal, while those with Pathogenic1 and Pathogenic2-containing worms are roaming defective (**Figure 2B**). Similar to the dye filling observations, VUS4, VUS5, VUS6, and to a lesser extent VUS1, cause a severe roaming defect (similar to *mks-3(Δ)*), whereas worms containing VUS2 and VUS3 are roaming normal (**Figure 2B**). VUS7-containing worms exhibit an intermediate roaming defect (**Figure 2B**).

C. elegans chemotaxis towards benzaldehyde, a volatile compound, is dependent on AWC sensory cilia [35]. To assay this behaviour, approximately 100 worms are placed in the center of a plate, equidistant from spots of applied control (ethanol) and benzaldehyde (ethanol diluted) solutions. *mks-3(+); nphp-4(Δ)* worms show a slight reduction in chemotaxis compared to wild type, whereas *mks-3(Δ); nphp-4(Δ)* worms exhibit a chemotaxis defective phenotype (**Figure 2C**). As expected, Benign1 and Benign2-containing strains are chemotaxis normal

356 (**Figure 2C**). Surprisingly, whilst worms with Pathogenic1 are strongly chemotaxis defective,
357 those with Pathogenic2 are not, a discrepancy that was consistent in all assay replicates
358 (**Figure 2C**). In agreement with the dye filling and roaming data, VUS4, VUS5, and
359 VUS6-containing strains are severely chemotaxis defective (similar to *mks-3(Δ)*), whereas
360 VUS2 or VUS3-containing worms are chemotaxis normal (**Figure 2C**). VUS1 and
361 VUS7-containing worms exhibit an intermediate phenotype (**Figure 2C**).
362
363 To derive a predictive 'interpretation' score for the VUS alleles, we integrated the results
364 from the three phenotypic assays into a single value (equal weighting, averages normalized to
365 the *mks-3(+); nphp-4(Δ)* control) (**Figure 2D**). As expected, the Benign1 (3.04) and Benign2
366 (2.97) variants score similarly to the *mks-3(+)* positive control (3.0), whereas Pathogenic1
367 (1.26) and Pathogenic2 (1.59) variants score similarly to the *mks-3(Δ)* negative control/null
368 (1.31) (**Figure 2D**). VUS2 (2.94) and VUS3 (2.74) received high scores comparable to the
369 benign variants, whereas VUS1 (1.65), VUS4 (1.40), VUS5 (1.12) and VUS 6 (1.03)
370 received scores comparable to the pathogenic variants. Therefore, we conclude that in the
371 context of *C. elegans mks-3* gene function, VUS2/3 are benign alleles whereas VUS1/4/5/6
372 are pathogenic alleles. VUS7 obtained an intermediate score (2.28) and the pathogenicity is
373 inconclusive.
374
375 **Effect of VUSs on TZ localization of MKS-3 and TZ ultrastructure**
376 To provide further insight into the damaging or benign nature of the VUS alleles, we
377 examined the effect of the variants on the subcellular localisation of MKS-3. MKS-3 is a
378 transmembrane protein that exclusively localizes to the ciliary transition zone in *C. elegans*[22].
379 We used fusion PCR to generate linear *mks-3::gfp* fragments, which were injected into
380 *mks-3(Δ)* worms to obtain transgenic strains expressing the constructs. PCR genotyping
381 confirmed that the *mks-3::gfp* constructs were present in the transgenic strains (**Figure S4A**).
382 A fluorescent lipophilic dye (DiI) was used to stain the ciliary membrane. As expected,
383 MKS-3(WT)::GFP, MKS-3(Benign1)::GFP, and MKS-3(Benign2)::GFP exhibit strong and
384 exclusive TZ localization in almost all analysed worms (**Figure 3A**). Notably, however,
385 quantification of signal intensities revealed 40% less MKS-3(Benign2)::GFP at the TZ
386 compared with the MKS-3(WT)::GFP and MKS-3(Benign1)::GFP (**Figure S4B**).
387 MKS-3(Pathogenic2)::GFP showed no detectable fluorescence at the TZ, consistent with the

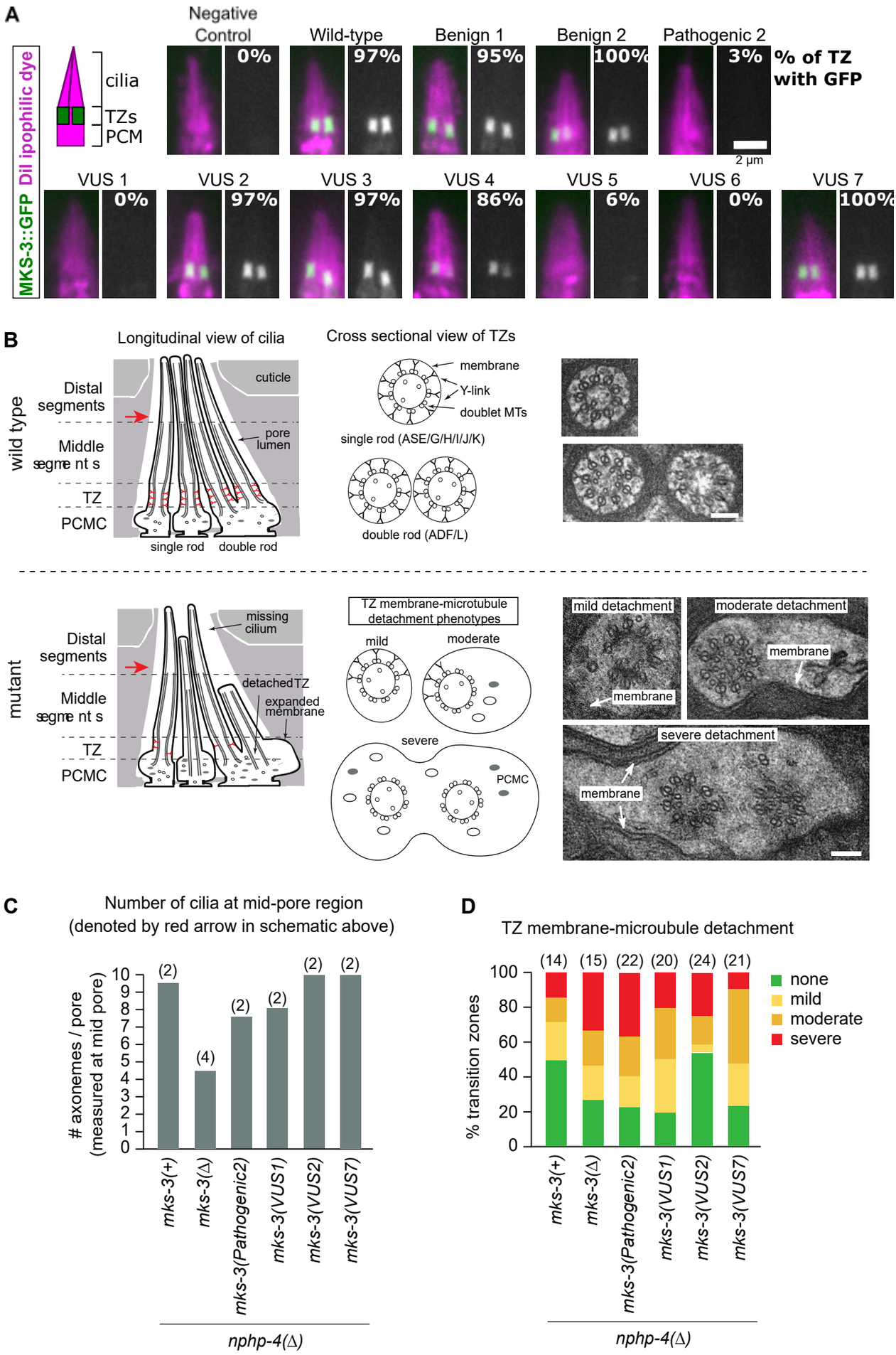

Figure 3. Testing mks-3 variant predictions via analysis of GFP reporter localization and cilia/transition zone ultrastructure

A) Transgenic worm strains containing MKS-3::GFP extrachromosomal array were generated in *mks-3(Δ)* genetic background. DiI (magenta) lipophilic dye stains the cilia and peri-ciliary membrane (PCM). Greyscale shows the green channel alone. The percent of cilia with MKS-3::GFP localized to the transition zone (TZ) is indicated. Pathogenic2, VUS1, VUS5, and VUS6 lack MKS-3::GFP localization to the transition zone. Scale bar is 2µm. B) Ultrastructure of amphid channel ciliary axonemes and the transition zone compartment in the indicated genotypes. Schematics show channel cilia in longitudinal orientation (only 4 of the 10 axonemes are shown for simplicity), and transition zones in radial orientation. Electron micrograph images show the TZs in cross section (scale bars; 100 nm). C) The mean number of cilia observed at the mid-pore region. D) TZ membrane-microtubule (MTs) detachment phenotypes of differing severity: mild - TZ MTs are slightly detached from the membrane, which is expanded to a small degree; moderate - many TZ MTs are clearly detached from the membrane, which is extensively expanded on one side of the axoneme; severe - most or all of the TZ MTs are fully detached from the

finding that the human Pathogenic2 mutation (Q376P) disrupts TMEM67 plasma membrane localization in cell culture[36]. Our initial interpretation that the VUS2 and VUS3 variants are benign predicts that the proteins should localize normally at the TZ. Consistent with this hypothesis, MKS-3(VUS2)::GFP and MKS-3(VUS3)::GFP display robust localization to the TZ, at levels similar to the MKS-3(WT)::GFP control (**Figure 3A, S4B**). In contrast, MKS-3(VUS1)::GFP, MKS-3(VUS5)::GFP, and MKS-3(VUS6)::GFP show no significant TZ localisation, consistent with these VUSs being pathogenic. Interestingly, despite a pathogenic prediction for VUS4, MKS-3(VUS4)::GFP was TZ-localized in most worms, although signal levels were reduced and varied compared to the MKS-3(WT)::GFP control reporter (**Figure 3A**). Finally, MKS-3(VUS7)::GFP shows relatively strong TZ localization similar to that of MKS-3(Benign2)::GFP.

We also assessed the effect of the VUS variants on the ultrastructure of amphid sensory cilia and TZs using transmission electron microscopy (TEM). Since TEM is labour intensive, we focussed on three VUSs that cover all our predictions, namely VUS1 (predicted pathogenic), VUS2 (predicted benign) and VUS7 (predicted uncertain). Pathogenic2 was also examined as a control. All analysed strains also contained the *nphp-4(Δ)* mutation, for reasons as outlined above. Wild type amphidal pores contain 10 rod-shaped ciliary axonemes from 8 sensory neurons (2 neurons possess a pair or rods), each consisting of middle (doublet microtubules) and distal (singlet microtubules) segments, and a proximal TZ compartment that emerges from a swelling at the distal dendrite tip called the periciliary membrane compartment (PCMC) (**Figure 3B**). First we assessed cross sections at the middle pore region, where middle segments transition to distal segments. *mks-3(+); nphp-4(Δ)* positive controls display an almost full complement of 10 cilia in this region, whereas at least two axonemes are missing in the *mks-3(Δ); nphp-4(Δ)* negative control and in Pathogenic2-containing worms (**Figure 3C**). For the VUSs, we found that VUS1-containing worms are also missing some axonemes, whereas VUS2- and VUS7-containing strains are not (**Figure 3C**). Next we examined cross-sections from the TZ and PCMC regions of rod and wing cilia. For the *mks-3(+); nphp-4(Δ)* positive control, approximately 50% of TZs show a wild type phenotype, with the TZ membrane and microtubules in close apposition, connected by electron dense Y-linkers (**Figure 3B)**. On account of the background *nphp-4(Δ)* mutation, and as previously reported[37], the remaining *mks-3(+)* TZs show varying degrees of

membrane-microtubule detachment, classified as mild, moderate or severe (**Figure 3B**). By comparison, the *mks-3(Δ); nphp-4(Δ)* negative control and the Pathogenic2-containing strain show a much more severe phenotype (**Figure 3D**). For the VUSs, the VUS2-containing strain displays a similar TZ phenotype to the positive control, whereas the VUS1 and VUS7-containing strains show enhanced TZ membrane-MT detachment phenotypes that are similar to the negative control (**Figure 3D**). Together, the ultrastructure data confirms the pathogenic and benign nature of VUS1 and VUS2, respectively. The TEM findings also confirm the uncertain nature of VUS7, which although not affecting amphid cilium length/position or number does affect TZ ultrastructure.

In vitro **genetic complementation assays of TMEM67 VUS function**

To further validate our findings from *C. elegans*, we utilized an *in vitro* human cell culture-based assay of potential pathogenic effects of *TMEM67* VUS. In this analysis, we also included VUS8(Ser961Tyr) which was not analyzed in worms. We have previously demonstrated that TMEM67 is required for phosphorylation of the ROR2 co-receptor and subsequent activation of non-canonical Wnt signalling[30] (**Figure 4A**). We developed a genetic complementation approach using a validated hTERT-RPE1 crispant cell-line that has biallelic null mutations in *TMEM67* (**Figure S5**). In the absence of TMEM67, phosphorylation of ROR2 could not be stimulated by exogenous treatment with the non-canonical ligand Wnt5a in comparison to control treatment. However, transient transfection with a construct that expresses full-length wild-type TMEM67 allowed the full rescue of ROR2 phosphorylation following Wnt5a treatment. These responses allowed us to develop a series of assays to determine the relative effects of VUS on biological function, based on the quantitation of phospho-ROR2 levels. In this assay, transfection of Benign1 allowed 204.7% induction of phospho-ROR2 levels by Wnt5a relative to control (**Figure 4B**). In contrast, Pathogenic2 did not rescue biological function (90.2% induction) (**Figure 4B**). Comparison of all VUS, normalized to wild-type TMEM67 responses across three independent biological replicates, enabled us to interpret VUS1, VUS4, VUS5, VUS6 and VUS8 as pathogenic; and VUS3 and VUS7 as benign (**Figure 4C**). VUS2 was not tested in this assay.

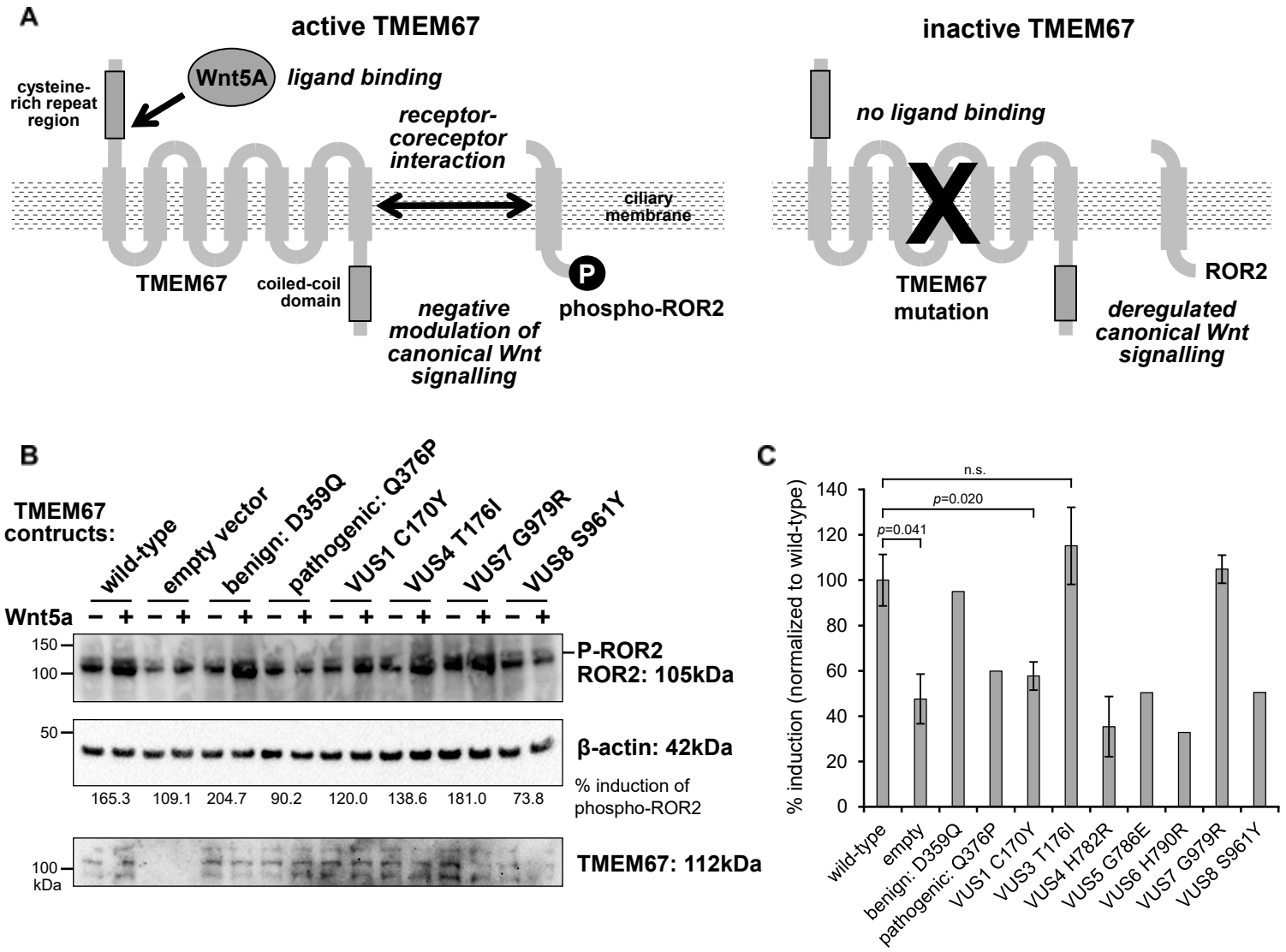

Figure 4. Validation of *C. elegans* predictions of TMEM67 VUS pathogenicity in cell culture

A) Schematic that summarizes the genetic complementation in hTERT-RPE1 *TMEM67* knock-out cells. Left: in the presence of TMEM67, phosphorylation of the co-receptor ROR2 is stimulated by exogenous treatment with the non-canonical ligand Wnt5a in comparison to control treatment. Right: if TMEM67 is lost or mutated, ROR2 phosphorylation is not stimulated by this treatment. However, transient transfection with a construct that expresses full-length wild-type TMEM67 allows the full rescue of ROR2 phosphorylation following Wnt5a treatment.

B) Western blots of ROR2, with upper phosphorylated isoform indicated (top panel), following transfection and expression (bottom panel) of TMEM67 constructs (wild-type, empty vector negative control, known benign variant control, known pathogenic mutation control, and a selection of VUS alleles). Transfected *TMEM67-/-* knock-out cells were treated with control conditioned medium (-) or Wnt5a-conditioned medium (+). Levels of -actin are the loading control.

C) Densitometry scans of the phosphorylated ROR2 isoform (for n=3 biological replicates) were quantitated in the bar graph for % induction of Wnt5a-stimulated response compared to control response, normalized against responses to the wild-type TMEM67 construct. Pair-wise comparisons indicate statistical tests (Student t-test) for a minimum of n=3 biological replicates (n.s. not significant) with error bars indicating s.e.m. All other error bars indicate range values for n=2 replicates.

449 **DISCUSSION**

450 Ciliopathies are multisystem disorders that affect many organs including kidneys, liver, and
451 retina. While the organ systems affected by cilia dysfunction are not conserved in *C. elegans*,
452 the basic cell biology of cilia function is conserved. In this study, we exploited efficient
453 genome editing and quantitative phenotypic analysis in *C. elegans* to predict the
454 pathogenicity of human *TMEM67* variants. This approach was able to accurately classify
455 known pathogenic and known benign variants. We were able to generate a pathogenicity
456 prediction for six of the seven (85.7%) VUS alleles analyzed. Two variants were
457 phenotypically benign: VUS2(Cys173Arg) and VUS3(Thr176Ile). Four VUS alleles were
458 severely defective in the cilia-dependent phenotypic assays: VUS1(Cys170Tyr),
459 VUS4(His782Arg), VUS5(Gly786Glu), and VUS6(His790Arg). These pathogenic
460 predictions were validated in a human cell culture assay of TMEM67 function.
461 VUS7(Gly979Arg), had an intermediate phenotype in *C. elegans* and it was unclear whether
462 the subtle defects were sufficient to be classified as pathogenic. In cell culture experiments,
463 VUS7 was functional which suggests that the worm assays may be very sensitive and detect
464 even subtle changes in cilia biology. Nuances in the phenotypes associated with specific
465 assays, such as the roaming and chemotaxis assays of VUS7, may highlight specific
466 biological consequences of this variant in future studies. The characterization of additional
467 pathogenic and benign variants will help to generate more comprehensive criteria for
468 pathogenicity and facilitate variant interpretation.
469
470 The analysis we used to predict the pathogenicity of the TMEM67/*mks-3* variants equally
471 weighted the results from the dye filling, roaming, and chemotaxis assays (**Figure 2D**). This
472 approach assumes that each assay has equal predictive power. However, some assays may be
473 more accurate than others. VUS7 was dye filling normal with slight defects in roaming and
474 chemotaxis assays; in the cell culture assay VUS7 was able to complement loss of TMEM67
475 suggesting that this allele is benign. These observations suggest that the dye filling assay may
476 be the more predictive of the three. If the dye filling assays is weighted more heavily in the
477 analysis then this variant would receive a benign score rather than inconclusive. Analysis of
478 additional alleles is required to firmly establish which assays are most predictive of *TMEM67*
479 variant pathogenicity.
480

481 We sought to compare our *in vivo* analysis with *in silico* predictions of the TMEM67
482 missense variants (**Figure S6**). In general, the *in silico* predictions of the TMEM67 VUS
483 alleles were deleterious or damaging. Several of these assays (MISTIC, SIFT, and CADD)
484 incorporate protein conservation in their prediction algorithms. Since we selected variants
485 that were conserved or in highly conserved regions, it is understandable that these algorithms
486 would predict that these variants are pathogenic. The only exception was VUS3 which was
487 predicted to be non-deleterious by CADD and has an intermediate score with Poly-Phen.
488 Overall, the algorithms we employed to predict the pathogenicity of the *TMEM67* missense
489 alleles did not align with our observations in *C. elegans*. VUS2 was phenotypically wild-type
490 in all assays tested, yet was predicted to be deleterious/damaging by all five algorithms
491 tested. VUS3 was also benign in all phenotypic assays but only CADD and Poly-Phen
492 predicted it was not deleterious. We did not find any correlation between phenotype severity
493 in worms and the various scores of deleteriousness. This is best exemplified by VUS7 which
494 had an intermediate phenotype in *C. elegans* and was functional in cell culture but was
495 ranked as the most severe allele by the prediction algorithms. We conclude that functional
496 modelling of missense variants in *C. elegans* more accurately predicts results in human cells
497 than currently available *in silico* prediction algorithms.
498
499 TMEM67/*mks-3* and B9D2/*mksr-2* are both components of the MKS module of transition
500 zone proteins. It is tempting to assume that variants in these superficially similar genes could
501 be analyzed with the same assays. In practice, this is not the case. While the osmotic assay
502 was excellent to quantify two B9D2/*mksr-2* pathogenic variants[20], it was not informative to
503 assess TMEM67/*mks-3* variants (**Figure S7**). This difference is likely due to the fact that
504 these genes have different functions at the TZ. This observation highlights that the most
505 predictive assays may be gene-specific and underscores the importance of empirically
506 determining which assays to utilize in interpreting variant pathogenicity.
507
508 The quantitative phenotypic assays employed in this study are suitable for high throughput
509 analysis. Live animal fluorescence-activated cell sorting can be used for high throughput dye
510 filling assays[38] and automated worm tracking can be used for high throughput roaming and
511 chemotaxis assays[39,40]. *C. elegans* are well suited for large-scale drug screens[41–44] and the
512 worm strains generated in this study could potentially be used in drug screens for ciliopathy

treatments. One limitation to modelling patient variants in *C. elegans* is the conservation of the specific amino acid residues. Although many TZ genes have clear orthologs in *C. elegans,* the amino acid conservation varies from 30-60%. *C. elegans* can be "humanized" with worm codon-optimized human cDNA[45,46] to remove this limitation and facilitate the interpretation of additional variants.

In summary, this study highlights how *C. elegans* is a practical model to interpret ciliopathy-associated variants of uncertain significance. Analysis of ciliopathy-associated VUS in *C. elegans* is accurate, quick, affordable, and easily interpretable. Efficient genome editing and the availability of assays to quantitatively assess cilia make *C. elegans* a convenient model to predict variant pathogenicity. Although this study focused on TMEM67, we anticipate that VUS alleles of any conserved ciliary genes can be modelled and characterized in *C. elegans*.

Acknowledgements

This work was funded by Science Foundation Ireland (SFI) in partnership with the Biotechnology and Biological Sciences Research Council (BBSRC) under grant number 16/BBSRC/3394 (to OEB) and BB/P007791/1 (to CAJ). SB acknowledges support from a Wellcome Trust clinical training fellowship (203914/Z/16/Z). We thank Joseph McNicholl for assistance with strain generation and analysis.

References

1. Splinter K, Adams DR, Bacino CA, et al. Effect of Genetic Diagnosis on Patients with Previously Undiagnosed Disease. *N Engl J Med*. 2018;379(22):2131-2139. doi:10.1056/NEJMoa1714458

2. Bachmann-Gagescu R, Dempsey JC, Bulgheroni S, et al. Healthcare recommendations for Joubert syndrome. *Am J Med Genet A*. 2020;182(1):229-249. doi:10.1002/ajmg.a.61399

3. Karczewski KJ, Francioli LC, Tiao G, et al. The mutational constraint spectrum quantified from variation in 141,456 humans. *Nature*. 2020;581(7809):434-443. doi:10.1038/s41586-020-2308-7

4. MacArthur DG, Balasubramanian S, Frankish A, et al. A systematic survey of loss-of-function variants in human protein-coding genes. *Science*. 2012;335(6070):823-828. doi:10.1126/science.1215040

5. Richards S, Aziz N, Bale S, et al. Standards and guidelines for the interpretation of sequence variants: a joint consensus recommendation of the American College of Medical Genetics and Genomics and the Association for Molecular Pathology. *Genet Med*. 2015;17(5):405-424. doi:10.1038/gim.2015.30

6. Ellard S, Baple EL, Berry I, Others. ACGS best practice guidelines for variant classification in rare disease 2020. *Assoc Clin Genomic Sci (ACGS)*. Published online 2020.

7. Weile J, Roth FP. Multiplexed assays of variant effects contribute to a growing genotype-phenotype atlas. *Hum Genet*. 2018;137(9):665-678. doi:10.1007/s00439-018-1916-x

8. Thusberg J, Olatubosun A, Vihinen M. Performance of mutation pathogenicity prediction methods on missense variants. *Hum Mutat*. 2011;32(4):358-368. doi:10.1002/humu.21445

9. Shulman C, Liang E, Kamura M, et al. Type IV Collagen Variants in CKD: Performance of Computational Predictions for Identifying Pathogenic Variants. *Kidney Med*. 2021;3(2):257-266. doi:10.1016/j.xkme.2020.12.007

10. Miosge LA, Field MA, Sontani Y, et al. Comparison of predicted and actual consequences of missense mutations. *Proc Natl Acad Sci U S A*. 2015;112(37):E5189-E5198. doi:10.1073/pnas.1511585112

11. Brnich SE, Abou Tayoun AN, Couch FJ, et al. Recommendations for application of the functional evidence PS3/BS3 criterion using the ACMG/AMP sequence variant interpretation framework. *Genome Med*. 2019;12(1):3. doi:10.1186/s13073-019-0690-2

12. Wangler MF, Yamamoto S, Chao H-T, et al. Model Organisms Facilitate Rare Disease Diagnosis and Therapeutic Research. *Genetics*. 2017;207(1):9-27.

573 doi:10.1534/genetics.117.203067

574 13. Baldridge D, Wangler MF, Bowman AN, et al. Model organisms contribute to diagnosis
575 and discovery in the undiagnosed diseases network: current state and a future vision.
576 *Orphanet J Rare Dis*. 2021;16(1):206. doi:10.1186/s13023-021-01839-9

577 14. Wheway G, Mitchison HM, Genomics England Research Consortium. Opportunities
578 and Challenges for Molecular Understanding of Ciliopathies-The 100,000 Genomes
579 Project. *Front Genet*. 2019;10:127. doi:10.3389/fgene.2019.00127

580 15. Waters AM, Beales PL. Ciliopathies: an expanding disease spectrum. *Pediatr Nephrol*.
581 2011;26(7):1039-1056. doi:10.1007/s00467-010-1731-7

582 16. Malicki JJ, Johnson CA. The Cilium: Cellular Antenna and Central Processing Unit.
583 *Trends Cell Biol*. 2017;27(2):126-140. doi:10.1016/j.tcb.2016.08.002

584 17. Satir P, Pedersen LB, Christensen ST. The primary cilium at a glance. *Journal of Cell*
585 *Science*. 2010;123(4):499-503. doi:10.1242/jcs.050377

586 18. Anvarian Z, Mykytyn K, Mukhopadhyay S, Pedersen LB, Christensen ST. Cellular
587 signalling by primary cilia in development, organ function and disease. *Nat Rev*
588 *Nephrol*. 2019;15(4):199-219. doi:10.1038/s41581-019-0116-9

589 19. Kim W, Underwood RS, Greenwald I, Shaye DD. OrthoList 2: A New Comparative
590 Genomic Analysis of Human and Caenorhabditis elegans Genes. *Genetics*.
591 2018;210(2):445-461. doi:10.1534/genetics.118.301307

592 20. Lange KI, Tsiropoulou S, Kucharska K, Blacque OE. Interpreting the pathogenicity of
593 Joubert Syndrome missense variants in Caenorhabditis elegans. *Dis Model Mech*.
594 Published online January 4, 2021. doi:10.1242/dmm.046631

595 21. Smith UM, Consugar M, Tee LJ, et al. The transmembrane protein meckelin (MKS3) is
596 mutated in Meckel-Gruber syndrome and the wpk rat. *Nat Genet*. 2006;38(2):191-196.
597 doi:10.1038/ng1713

598 22. Williams CL, Masyukova SV, Yoder BK. Normal ciliogenesis requires synergy between
599 the cystic kidney disease genes MKS-3 and NPHP-4. *J Am Soc Nephrol*.
600 2010;21(5):782-793. doi:10.1681/ASN.2009060597

601 23. Tallila J, Salonen R, Kohlschmidt N, Peltonen L, Kestilä M. Mutation spectrum of
602 Meckel syndrome genes: one group of syndromes or several distinct groups? *Hum*
603 *Mutat*. 2009;30(8):E813-E830. doi:10.1002/humu.21057

604 24. Domingo-Gallego A, Pybus M, Bullich G, et al. Clinical utility of genetic testing in
605 early-onset kidney disease: seven genes are the main players. *Nephrol Dial Transplant*.
606 Published online February 3, 2021. doi:10.1093/ndt/gfab019

607 25. Vogel I, Ott P, Lildballe D, Hamilton-Dutoit S, Vilstrup H, Grønbæk H. Isolated
608 congenital hepatic fibrosis associated with TMEM67 mutations: report of a new
609 genotype-phenotype relationship. *Clin Case Rep*. 2017;5(7):1098-1102.

610 doi:10.1002/ccr3.981

611 26. Landrum MJ, Lee JM, Benson M, et al. ClinVar: improving access to variant
612 interpretations and supporting evidence. *Nucleic Acids Res*. 2018;46(D1):D1062-D1067.
613 doi:10.1093/nar/gkx1153

614 27. Brenner S. The genetics of Caenorhabditis elegans. *Genetics*. 1974;77(1):71-94.
615 https://www.ncbi.nlm.nih.gov/pubmed/4366476

616 28. Sanders AAWM, Kennedy J, Blacque OE. Image analysis of Caenorhabditis elegans
617 ciliary transition zone structure, ultrastructure, molecular composition, and function.
618 *Methods Cell Biol*. 2015;127:323-347. doi:10.1016/bs.mcb.2015.01.010

619 29. Hobert O. PCR fusion-based approach to create reporter gene constructs for expression
620 analysis in transgenic C. elegans. *Biotechniques*. 2002;32(4):728-730.
621 doi:10.2144/02324bm01

622 30. Abdelhamed ZA, Natarajan S, Wheway G, et al. The Meckel-Gruber syndrome protein
623 TMEM67 controls basal body positioning and epithelial branching morphogenesis in
624 mice via the non-canonical Wnt pathway. *Dis Model Mech*. 2015;8(6):527-541.
625 doi:10.1242/dmm.019083

626 31. Xu J. Distance-based protein folding powered by deep learning. *Proc Natl Acad Sci U S*
627 *A*. 2019;116(34):16856-16865. doi:10.1073/pnas.1821309116

628 32. Hunt SE, McLaren W, Gil L, et al. Ensembl variation resources. *Database* . 2018;2018.
629 doi:10.1093/database/bay119

630 33. Starich TA, Herman RK, Kari CK, et al. Mutations affecting the chemosensory neurons
631 of Caenorhabditis elegans. *Genetics*. 1995;139(1):171-188.
632 https://www.ncbi.nlm.nih.gov/pubmed/7705621

633 34. Perkins LA, Hedgecock EM, Nichol Thomson J, Culotti JG. Mutant sensory cilia in the
634 nematode Caenorhabditis elegans. *Developmental Biology*. 1986;117(2):456-487.
635 doi:10.1016/0012-1606(86)90314-3

636 35. Bargmann CI, Hartwieg E, Horvitz HR. Odorant-selective genes and neurons mediate
637 olfaction in C. elegans. *Cell*. 1993;74(3):515-527. doi:10.1016/0092-8674(93)80053-h

638 36. Dawe HR, Smith UM, Cullinane AR, et al. The Meckel-Gruber Syndrome proteins
639 MKS1 and meckelin interact and are required for primary cilium formation. *Hum Mol*
640 *Genet*. 2007;16(2):173-186. doi:10.1093/hmg/ddl459

641 37. Lambacher NJ, Bruel A-L, van Dam TJP, et al. TMEM107 recruits ciliopathy proteins to
642 subdomains of the ciliary transition zone and causes Joubert syndrome. *Nat Cell Biol*.
643 2016;18(1):122-131. doi:10.1038/ncb3273

644 38. Fernandez AG, Bargmann BOR, Mis EK, Edgley ML, Birnbaum KD, Piano F.
645 High-throughput fluorescence-based isolation of live C. elegans larvae. *Nat Protoc*.
646 2012;7(8):1502-1510. doi:10.1038/nprot.2012.084

39. Swierczek NA, Giles AC, Rankin CH, Kerr RA. High-throughput behavioral analysis in C. elegans. *Nat Methods*. 2011;8(7):592-598. doi:10.1038/nmeth.1625

40. Churgin MA, Fang-Yen C. An Imaging System for C. elegans Behavior. *Methods Mol Biol*. 2015;1327:199-207. doi:10.1007/978-1-4939-2842-2_14

41. Kukhtar D, Rubio-Peña K, Serrat X, Cerón J. Mimicking of splicing-related retinitis pigmentosa mutations in C. elegans allow drug screens and identification of disease modifiers. *Hum Mol Genet*. 2020;29(5):756-765. doi:10.1093/hmg/ddz315

42. Iyer S, Mast JD, Tsang H, et al. Drug screens of NGLY1 deficiency in worm and fly models reveal catecholamine, NRF2 and anti-inflammatory-pathway activation as potential clinical approaches. *Dis Model Mech*. 2019;12(11). doi:10.1242/dmm.040576

43. Patten SA, Aggad D, Martinez J, et al. Neuroleptics as therapeutic compounds stabilizing neuromuscular transmission in amyotrophic lateral sclerosis. *JCI Insight*. 2017;2(22). doi:10.1172/jci.insight.97152

44. Gosai SJ, Kwak JH, Luke CJ, et al. Automated high-content live animal drug screening using C. elegans expressing the aggregation prone serpin α1-antitrypsin Z. *PLoS One*. 2010;5(11):e15460. doi:10.1371/journal.pone.0015460

45. McDiarmid TA, Au V, Loewen AD, et al. CRISPR-Cas9 human gene replacement and phenomic characterization in Caenorhabditis elegans to understand the functional conservation of human genes and decipher variants of uncertain significance. *Dis Model Mech*. 2018;11(12). doi:10.1242/dmm.036517

46. Zhu B, Mak JCH, Morris AP, et al. Functional analysis of epilepsy-associated variants in STXBP1/Munc18-1 using humanized Caenorhabditis elegans. *Epilepsia*. 2020;61(4):810-821. doi:10.1111/epi.16464